Applied Surface Science 545 (2021) 148962

Contents lists available at ScienceDirect

Applied Surface Science

journal homepage: www.elsevier.com/locate/apsusc

Full Length Article

Experimental and computational studies of sonochemical assisted anchoring of carbon quantum dots on reduced graphene oxide sheets towards the photocatalytic activity

M.G. Ashritha [a], Sachin R. Rondiya [b], Russell W. Cross [b], Nelson Y. Dzade [b], S.D. Dhole [c], K. Hareesh [a,*], D.V. Sunitha [a]

[a] School of Applied Sciences (Physics), REVA University, Bengaluru 560064, India
[b] School of Chemistry, Cardiff University, Main Building, Park Place, Cardiff CF10 3AT, Wales, United Kingdom
[c] Department of Physics, Savitribai Phule Pune University, Pune 411007, India

ARTICLE INFO

Keywords:
Carbon quantum dots
Reduced graphene oxide
Sonochemical method
Photocatalytic activity
Density functional theory

ABSTRACT

Herein, carbon quantum dots (CQDs) are anchored on reduced graphene oxide (rGO) sheets by sonochemical assisted method. The developed carbon quantum dots/reduced graphene oxide (CQDs/rGO) catalyst shows enhancement in the photocatalytic degradation of methylene blue and methyl orange under visible light compared to that of individual CQDs and rGO components. The improved performance of the CQDs/rGO catalyst has been attributed to efficient separation of photogenerated charge carriers as studied by photoluminescence studies and to increase in the surface area as studied by Brunauer-Emmett-Teller method. The photocatalytic degradation is studied in detail by varying catalyst loading, dye concentration and the rate constant is determined by first order kinetics. The enhancement in photocatalytic activity of CQDs/rGO catalyst is validated by first principles density functional theory (DFT) calculations which shows the enrichment in density of states thereby decreasing the work function.

1. Introduction

Carbon quantum dots, a zero dimensional nanomaterials with size less than 10 nm, have attracted significant research attenton because of their fascinating electronic properties, low toxicity, chemical inertness, good solubility, tunable fluorescence, easy surface modification, resistance to photo bleaching etc. [1–3]. These germane physicochemical properties have been explored for a wide range potential applications, including in catalysis [4], sensors [5], optronics [6], bioimaging [7], bio medicine [8]. Researchers have synthesized CQDs by various methods viz. hydrothermal [9], solvothermal [10], chemical ablation [11], laser ablation [12], microwave radiation [13], and sonochemical method [14]. Among all these methods, sonochemical assisted method has many advantages as it has fast reduction rate, environmental friendly, very small clusters can be produced and, it does not require any additional reducing agents, temperature, pressure [3,15]. Sonochemical assisted method uses acoustic cavitation phenomenons such as the formation, growth and impulsive collapse of bubbles [14,15]. In the context of sonochemical synthesis of CQDs, Liu et al., [16] have synthesized narrowly distributed CQDs of diameter in the range of (1.5–2.5) nm using ultrasonication. The monodispersed water soluble CQDs of size less than 5 nm were synthesized by Li [17] et al., using glucose by ultrasonic method. Kumar et al., [18] have reported the synthesis of CQDs with an average diameter of (2–9) nm using polyethylene glycol as a precursor by sonochemical method. The spherical CQDs of an average size of around 10 nm were synthesized by Maruthapandi et al., [19] using a sonochemical assisted method at 70 °C. In situ sonochemical method was used for the synthesis of Sn@C-dots and hybrid Sn@C-dots@Sn by Kumar et al. [20] with carbon dots of an average size of 5 nm at 75 °C. Kumar et al. [21] have prepared about (3–7) nm size of disc shape carbon dots using polyethylene glycol under a sonochemical assisted method with different amplitudes. Wei et al. [22] have studied the sonochemical method synthesis of highly photoluminescent CQDs of size (3–7) nm which exhibited high quantum yield and excellent photostability.

Nevertheless, the good luminescence property of CQDs will make the electron and hole to recombine soon thereby decreasing the photocatalytic activity of CQDs under visible light. This drawback can be

* Corresponding author.
E-mail address: appi.2907@gmail.com (K. Hareesh).

https://doi.org/10.1016/j.apsusc.2021.148962
Received 21 September 2020; Received in revised form 24 November 2020; Accepted 5 January 2021
Available online 7 January 2021

overcome by anchoring CQDs on some conducting two dimensional sheets such as graphene so that the generated electrons and holes can be efficiently separated [23]. Graphene is a two dimensional, monolayer of carbon atoms arranged in a honeycomb structure. Reduced graphene oxide (rGO) being an analogue of graphene, produced by removing oxygen functional groups viz. epoxy, carboxyl and hydroxyl groups from graphene oxide (GO) [24]. The reduction of GO to rGO can be done by many methods such as thermal, hydrazine, hydrothermal, green, irradiation and sonochemical method [25,26]. The impulsive collapse of bubbles which are produced during acoustic cavitation of sonochemical method will remove the oxygen functional groups from GO thereby forming rGO at no cost of any harsh reducing agent and high temperature [27]. The so produced rGO was anchored by various kinds of nanoparticles to use them as sensor [28], solar cell [29], electrochemical detection [30], supercapacitor [31] and catalyst [32]. Recently, few researchers have anchored CQDs on rGO to use them as supercapacitor [33], fluorescencents [34] and electrocatalyst [35]. Nevertheless, as per our knowledge, there is no report for the synthesis and simultaneous anchoring of CQDs on rGO sheets, and its application as photocatalyst under visible light.

Therefore, herein, the CQDs/rGO nanocomposite, CQDs and rGO were synthesized by sonochemical assisted method. The as prepared CQDs/rGO nanocomposite was characterized by high resolution transmission electron microscopy (HRTEM), X-ray diffractogram (XRD), Raman spectroscopy, X-ray photoelectron spectroscopy (XPS), photoluminescence (PL) spectroscopy, UV–Visible spectroscopy and the surface area was measured by Brunauer-Emmett-Teller method. The developed CQDs/rGO catalyst was applied to study the photocatalytic activity for the degradation of MB (basic) dye and MO (acidic) dye under sun light. Also, the detailed photocatalytic degradation was studied by varying catalyst loading and initial concentration of dye, and the reaction rate constant of catalysts were determined using first order kinetics. Further, the photocatalytic activity of CQDs/rGO catalyst was validated by theoretically calculated density of states and work function using first principles density functional theory methods.

2. Experimental section

2.1. Materials

Glucose, polyethylene glycol, methylene blue, methyl orange and chemicals used for the synthesis of graphene oxide were procured from Sigma Aldrich. Other chemicals used were of analytical grade, unless specified. Throught out the experiments Milli-Q water was used.

2.2. Sonochemical assisted synthesis of CQDs/rGO nanocomposite

The modified Hummers' method was used for the preparation of graphene oxide from graphite and the synthesis route is explained elsewhere [36]. The GO with concentration of 0.25 mg/mL was prepared by dispersing it in distilled water and sonicated for 30 min. 15 ml of aqueous solution containing 0.4 M of glucose and 1 M of polyethylene glycol was added to 30 ml of GO, and stirred for 30 min. Then, the solution was probe sonicated by inserting ultrasonic transducer ~2 cm above the bottom of test tube for 3 h with sonication amplitude as 60% using LABMAN PRO-250 Ultrasonicator having power 250 W. The unreacted precursors of the sample were removed by centrifugation (REMI R-4C) at 10,000 RPM for 20 min and the precipitate was collected. By changing the Milli-Q water for 3 days for every 24 h, the collected precipitate was further purified with the help of a 1 kda dialysis membrane. Then, CQDs/rGO nanocomposite was obtained through freeze drying of dialyzed solution. Similarly CQDs and rGO was synthesized without GO and CQDs precursors respectively. The schematic representation of formation of CQDs/rGO nanocomposite by sonochemical assisted method is shown in Scheme 1. During sonochemical synthesis, ultrasonic radiation will create organic radicals by cavitation bubbles and pyrolysis caused the carbonization of glucose forming CQDs [2] and also removes oxygen functional groups from GO forming rGO [37,38]. Typically, individual rGO sheets interacts via Van der waal's forces and π-π stacking resulting in the aggregation of rGO sheets [36]. Nonetheless, the formed CQDs will get embedded in between rGO sheets preventing its agglomeration, thereby increasing the surface area of CQDs/rGO nanocomposite which is supported by BET analysis as explained in Section 3.1. In turn, rGO sheets serve as stabilizers for CQDs results in the uniform distribution of CQDs over rGO sheets and is corroborated by TEM results as explained in Section 3.1.

2.3. Characterizations and apparatus

TEM images of CQDs and CQDs/rGO were imaged using FEI Technai T20 instrument at an accelerating voltage of 200 kV. The UV–Visible absorption spectrum were done using JASCO, V-670 spectrophotometer. XRD patterns were recorded by Bruker AXS D8 Advance X-Ray Diffractometer with Cu Kα radiation of wavelength 1.5406 Å. The Raman microscope of model Renishaw Invia with laser of excitation wavelength of 532 nm was used to record Raman spectra. XPS analysis

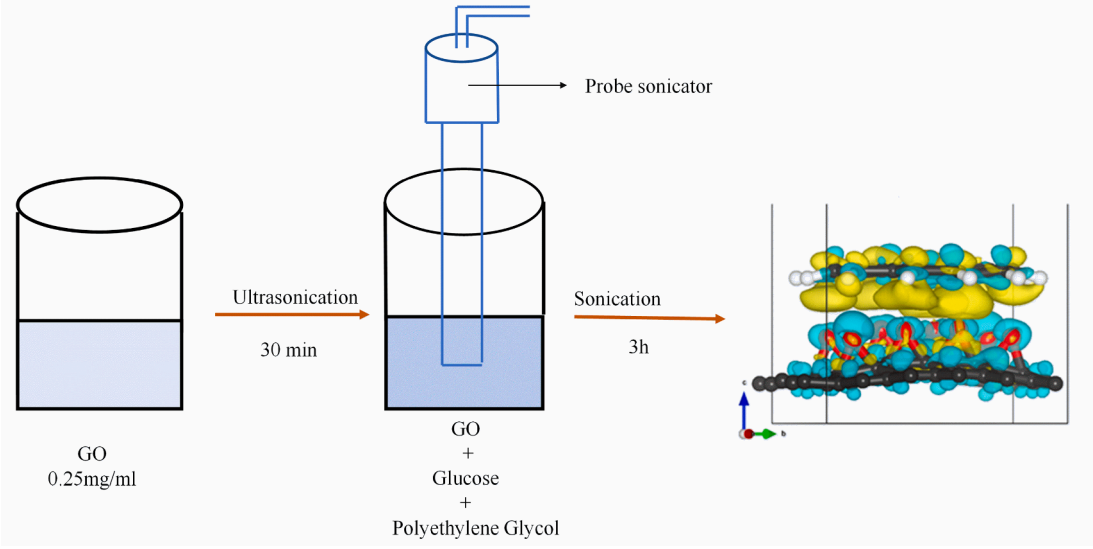

Scheme 1. The schematic representation of sonochemical assisted synthesis of CQDs/rGO nanocomposite.

was done using Perkin Elmer Model PHI 1257 using Mg K_{α}. The Perkin Emler, LS 55 photometer was used to carry out photoluminescence studies at room temperature. The surface area was found by Brunauer-Emmett-Teller (BET) method using Quantachrome, Autosorb iQ2.

2.4. DFT calculations

Vienna Ab initio Simulation Package (VASP), [39–41], a package which uses periodic plane wave DFT code for the interactions between valence as well as core electrons by Project Augmented Wave (PAW) [42] method was used for the first principle calculation of DFT. For the Kohn-Sham (KS) valence states a 600 eV cut-off kinetic energy was used. Till the relaxed atoms reached 10^{-3} eV $Å^{-1}$ of residual Hellmann–Feynman forces, based on the conjugate-gradient algorithm, geometrical optimization was done. The Perdew–Burke–Ernzerhof (PBE) generalized gradient approximation (GGA) functional [43] was

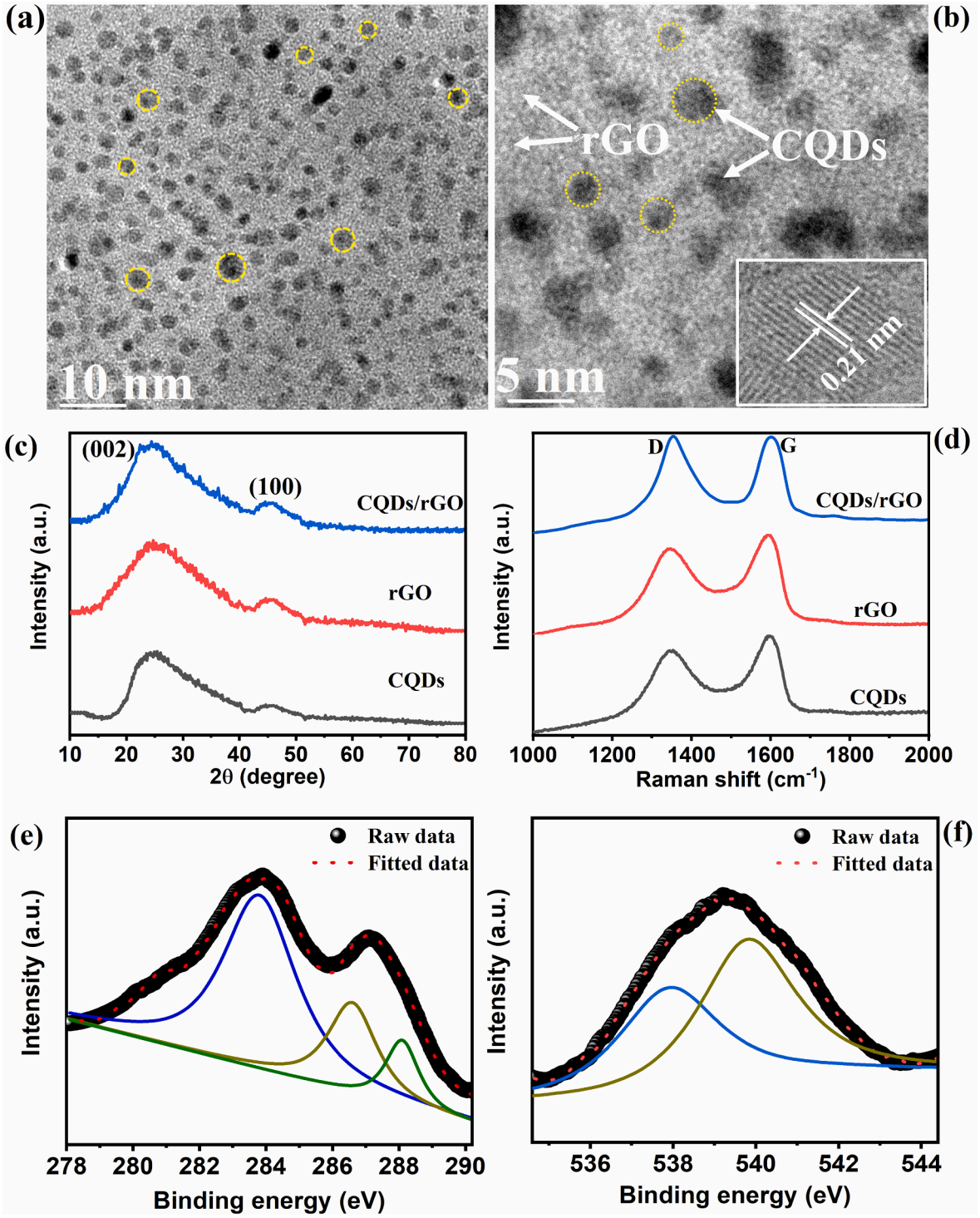

Fig. 1. TEM of (a) CQDs, (b) CQDs/rGO (Yellow dotted circles represents CQDs); (c) XRD, (d) Raman spectrum of CQDs, rGO & CQDs/rGO; high resolution XPS of (e) C1s & (f) O1s of CQDs/rGO. Inset of Fig. 1(b) shows the HRTEM of CQDs in CQDs/rGO. (For interpretation of the references to color in this figure legend, the reader is referred to the web version of this article.)

effectively used for the calculation of electronic exchange–correlation potential. The rGO monolayer was modelled with epoxide functional groups with 16% oxygen contents shown in Fig. 3(b). The isolated CQDs was modelled with a graphene hexagonal flake in a 25 × 25 × 25 Å^3 of orthorhombic dimension which contained 7 hexagons. As shown in Fig. 3(b), hydrogen atom saturated the edge atoms i.e., $C_{24}H_{12}$. Brillouin zones of the isolated rGO, CQDs, and CQDs/rGO are sampled using a *k*-point mesh of 5 × 5 × 1 dimension. With the exchange value of about 25% in screened hybrid functional HSE06 [44] was used to accurately predict the electronic structures of the isolated CQDs, rGO and the CQDs/rGO heterostructure. With the help of Bloch correction [27] by utilising a tetrahedron method, projected density of states (PDOS) was effectively calculated.

2.5. Photocatalytic activity of CQDs/rGO nanocomposite

The photocatalytic activity of CQDs/rGO, CQDs and rGO catalyst was studied towards the degradation of dyes such as methylene blue and methyl orange separately under sun light. 100 ml of dye was mixed with 2 mg of CQDs/rGO catalyst with continuous stirring for 20 min under dark condition to attain proper adsorption–desorption equilibrium. Then, the solution was exposed to sunlight with sunshine intensity as ~850 W/m^2 at coordinate 18°31′13″N, 73°51′24″E. 2 ml of solution was taken out from reaction mixture and its absorbance spectrum was recorded at the regular interval of 10 min. In a similar way, photocatalytic experiment was recorded for CQDs and rGO separately. To study the cyclic stability test of CQDs/rGO catalyst, the catalyst was recovered by centrifugation after the complete degradation of dye and washed several times by copious amount of MQ water. Then, XRD pattern was recorded for recovered CQDs/rGO catalyst and the aforesaid procedure of photocatalytic activity was repeated. The detailed photocatalytic degradation was studied by varying the catalyst loading (1 mg, 2 mg, 3 mg and 4 mg) and dye concentration (25 ppm, 50 ppm, 75 ppm and 100 ppm). The performance of photocatalysts was studied by plotting the graph of C/C_0 versus time, where C is concertation of (dye + catalyst) at time 't' and C_0 is concentration of dye at time '0'.

3. Results and discussions

3.1. Physico-chemical properties of CQDs/rGO nanocomposite

Fig. 1(a) & (b) show the TEM images of CQDs and CQDs/rGO nanocomposite, respectively. The TEM image in Fig. 1(a) indicated that the CQDs have good dispersity and particle size varied from 2 nm to 5 nm. The TEM image of CQDs/rGO displayed in Fig. 1(b), show the successful anchoring and distribution of CQDs uniformly on two dimensional rGO sheet. The inset of Fig. 1(b) depicts that the individual CQDs anchored on rGO had interlayer spacing of 0.21 nm which is nearby to the (1 0 0) plane of diffraction facet of graphite [33] corroborating XRD results. Fig. 1(c) depicts the XRD pattern of CQDs, rGO and CQDs/rGO nanocomposite, and that of GO is represented in Fig. S1 (a). GO displayed its characteristic peak around 10.52° corresponding to (0 0 1) plane. Furthermore, this peak vanisheed in CQDs/rGO with appearance of a broad and weak peak at 25° and 45°respectively corresponding to (0 0 2) plane (d_{002} = 0.36 nm) and (1 0 0) planes (d_{100} = 0.20 nm) [33].

The d-spacing (interlayer spacing) of (1 0 0) plane of CQDs/rGO nanocomposite was supported by HRTEM results. Even, CQDs and rGO also showed the same peaks confirming the presence of graphitic hexagonal structure . Further, the carbon structures of CQDs/rGO were confirmed by Raman spectra as depicted in Fig. 1(d) and, that of graphite and GO is displayed in Fig. S1 (b). The characteristics peaks of CQDs and rGO were observed at 1326 cm^{-1} and 1591 cm^{-1} corresponding to D and G band, respectively. The slight blue shift of D band in CQDs/rGO compared to rGO and CQDs was may be due to quantum confinement effect as explained in literature [33,34]. Also, the G band of CQDs/rGO was broadened ascribed to the enhancement in isolated double bonds and D band became outstanding due to enhanced disorder [45]. GO also showed D and G band at 1326 cm^{-1} and 1591 cm^{-1} respectively as displayed in Fig. S1(b). Nevertheless, the D band intensity of CQDs/rGO observed to be slightly more compared to CQDs and rGO. The disorder parameter in carbon based materials is determined using I_D/I_G ratio (a ratio of intensities of D band to corresponding G band) [35], and it was found to be 0.85, 0.89, 0.91 and 1.08 for GO, CQDs, rGO and CQDs/rGO, respectively. Among all, CQDs/rGO nanocomposite showed larger I_D/I_G ratio revealing the establishment of small sp^2 domains in larger number [35]. The surface composition of CQDs/rGO was examined using XPS and the corresponding survey scan is shown in Fig. S1 (c), which manifests the peaks at 285 eV due to C1s and 540 eV due to O1s. The high resolution XPS spectra is shown in Fig. 1(e) representing C1s of CQDs/rGO. It exhibited a strong as well as a peak around 284.0 eV and 287.0 eV respectively which were further deconvoluted into peaks at 283.9 eV which corresponding to sp^2, and at 286.5 eV and 288.0 eV corresponding to C-O and C═O respectively. The appearance of oxygen functional groups indicates the surface passivation and hydrophilic nature of synthesized CQDs in CQDs/rGO [46]. In order to study this further, the high resolution XPS of O1s was studied and is displayed in Fig. 1(f). It showed a broad peak around 539.0 eV, which is again deconvoluted into two peaks at 537.9 eV and 539.8 eV ascribed to C-O and C-O-C confirming the surface passivation of synthesized CQDs in CQDs/rGO nanocomposite. The surface passivation via these oxygen functional groups may be essential for the enhancement in luminescence properties of CQDs [3]. The PL (emission) spectra of CQDs, rGO and CQDs/rGO nanocomposite excited at 390 nm is displayed in Fig. 2(a). It can be witnessed from Fig. 2(a) that the CQDs showed a broad emission PL peak centered at 447 nm indicating the fast radiative recombination which arises due to the surface passivation as explained above. Nonetheless, the PL intensity of CQDs/rGO decreased compared to CQDs due to the prominent quenching effect indicating the effective charge transfer at the interface of CQDs and rGO [23]. Moreover, the sonochemical assisted reduction of GO restores the π conjugation between the carbon atoms and results in the formation of small sp^2 domains which percolate to facilitate the charge carrier transport by convenient extra path thereby disrupting radiation recombination, in turn enhancing the efficacy of photogenerated charge carriers. Fig. 2(b) depicts the UV–Visible absorption spectra of CQDs, rGO and CQDs/rGO nanocomposite, and that of GO is shown in Fig. S2(a). GO exhibited peaks at 232 nm and 290 nm corresponding to π-π* as well as n-π* transition of C═C bonds [4]. These peaks vanished for rGO (shown in Fig. 2(b)) and a broad peak appeared around 270 nm due to the formation of rGO [47]. Nevertheless, CQDs/rGO showed (in Fig. 2(b)) a shoulder peak around 270 nm and a broad peak around 340–410 nm which are the characteristic peak of rGO and CQDs respectively. Furthermore, it is observed that the CQDs/rGO showed a slight red shift compared to CQDs and rGO may be due to the decrease in its band gap. Hence, the band gap was found using equation $(\alpha h\nu)^n = A(h\nu - E_g)$, where α is absorption coefficient, A is a parameter that is related to effective masses associated with valence and conduction bands, n = ½ for direct transition, $h\nu$ is absorption energy and E_g is band gap [48]. The corresponding plot of $(\alpha h\nu)^{1/2}$ versus $h\nu$ for CQDs, rGO and CQDs/rGO are shown in Fig. 2(c). The band gap of CQDs and rGO were found to be 3.23 eV and 1.32 eV respectively, while that of CQDs/rGO was found to be 1.17 eV. The effective decrement in band gap of CQDs/rGO was attributed to synergetic effects of individual components making it a promising photocatalyst for solar driven applications. The UV–Visible spectroscopic results along with TEM, XRD, Raman spectroscopy, XPS results confirmed the anchoring of CQDs on rGO sheets. Furthermore, the surface structural properties such as surface area of nanocomposite was found using BET method and the corresponding nitrogen adsorption–desorption curves are displayed in Fig. 2(d). The surface area of rGO, CQDs and CQDs/rGO was found to be 115 m^2/g, 208 m^2/g and 296 m^2/g respectively. The enhancement in surface area of CQDs/rGO

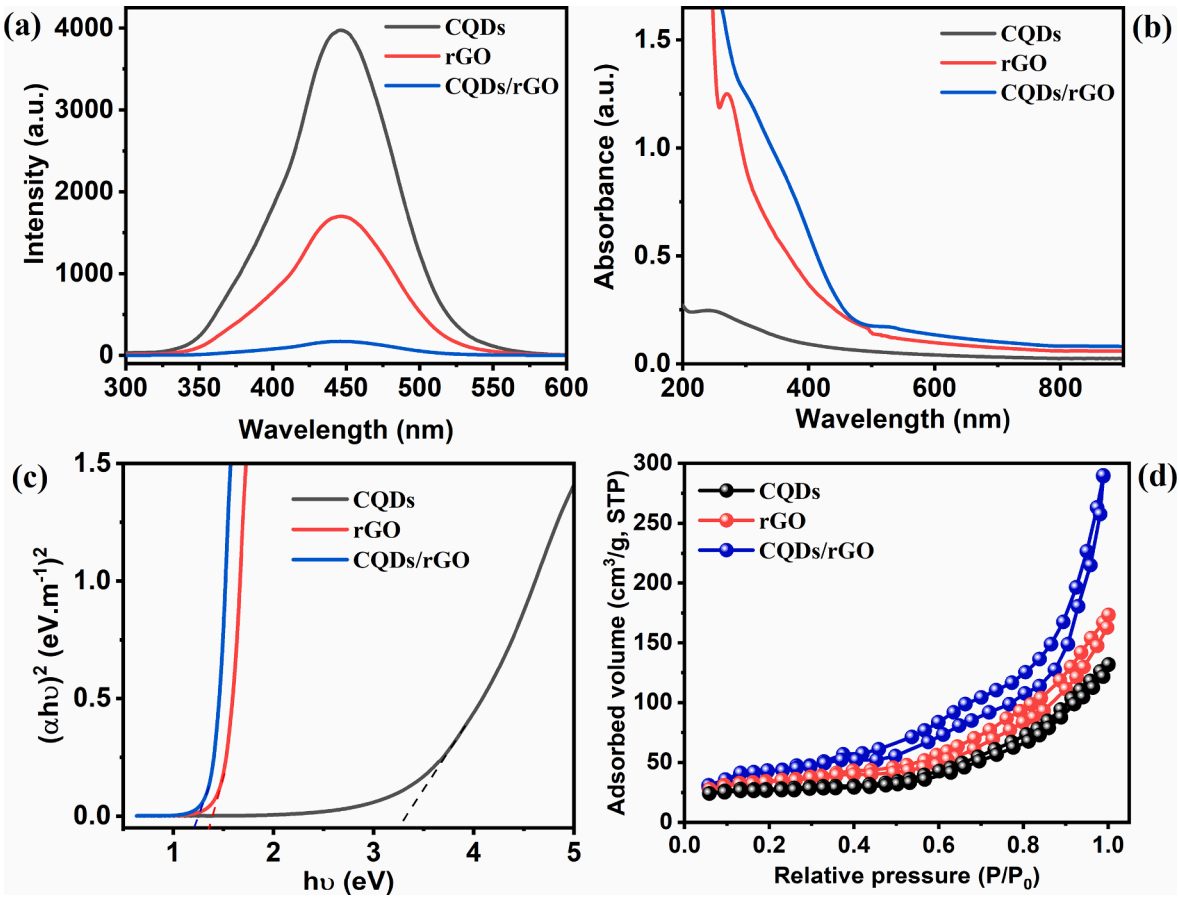

Fig. 2. (a) PL, (b) UV–Visible absorption spectrum, (c) Tauc's plot and (d) Nitrogen adsorption–desorption curves of CQDs, rGO and CQDs/rGO.

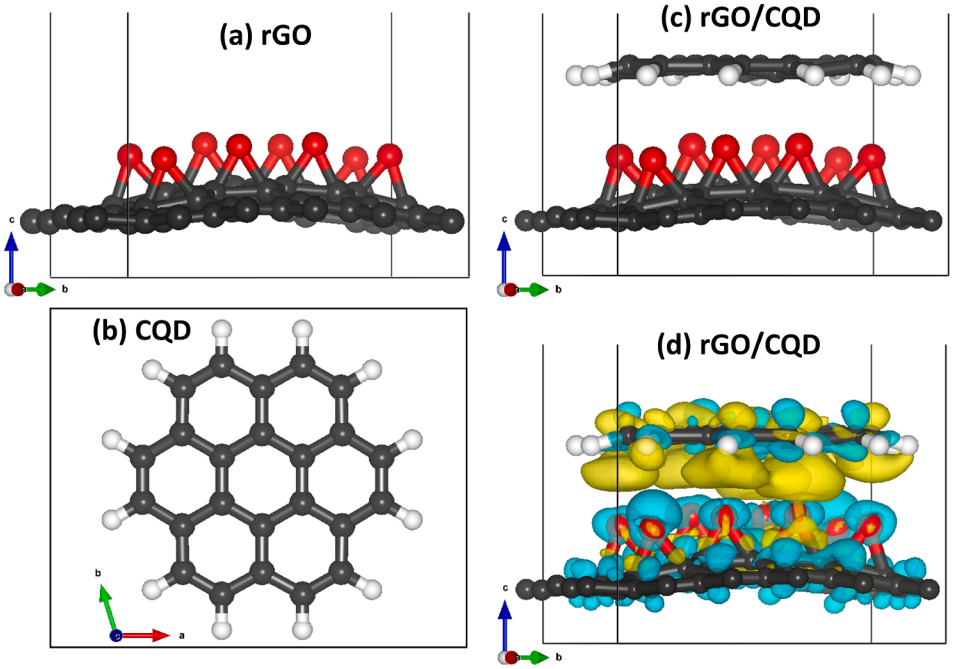

Fig. 3. Optimized structure of (a) rGO with epoxide functional group, (b) CQDs, (c) CQDs/rGO heterostructure and (d) the corresponding differential charge density isosurface contours. The yellow and cyan regions indicate electron density depletion and accumulation by 0.005 e/Å^3, respectively. Atomic color: C = grey, O = oxygen, H = white. (For interpretation of the references to color in this figure legend, the reader is referred to the web version of this article.)

was due to anchoring of CQDs which prevent the restacking of rGO sheets. Further, the rGO sheets may avoid the agglomeration of CQDs which in turn increase the surface area of CQDs/rGO nanocomposite validating the explanation given in Section 2.2.

3.2. DFT simulated results of CQDs/rGO nanocomposite

Atomic-level insights about electronic structure as well as work function (Φ) of the rGO, CQDs and CQDs/rGO were calculated using First-principles DFT by considering that they dictate their photocatalytic activity. The rGO monolayer was modelled with epoxide functional groups with 16% oxygen contents shown in Fig. 3(a). The isolated CQDs was modelled with a graphene hexagonal flake in a 25 × 25 × 25 $Å^3$ of orthorhombic dimension which contained 7 hexagons. As shown in Fig. 3(b), hydrogen atom saturated the edge atoms i.e., $C_{24}H_{12}$. We observed small disruptions in the two-dimensional honeycomb lattice, with the C atoms forming the epoxide functional groups are pulled upward in the z-direction (Fig. 3a). Compared to the rGO, the two-dimensional honeycomb lattice of the CQDs is essentially preserved (Fig. 3b). In the CQDs/rGO heterostructure (Fig. 3c), the interactions between the CQDs and rGO resulted in small disruption of the CQDs monolayer, with C atoms closest to O atoms of the rGO (d = 2.301 Å) pulled slightly downwards. We noticed that electron density accumulations in CQDs/rGO heterostructure is mainly in their interfacial bonding regions (Fig. 3d), suggesting electronic interactions between the CQDs and rGO layers, which gave rise to modulation of the electronic properties. From the projected density of states (Fig. 4), the band gap of rGO (Fig. 4(a)) and CQDs (Fig. 4(b)) monolayers is predicted at 0.81 and 2.01 eV, respectively [49]. Due to the electronic interactions between the CQDs and rGO in the CQDs/rGO heterostructure (Fig. 3(d) and 4(c)), the band gap is significantly reduced to 0.36 eV. Consistently, we observed a reduction in the work function for the CQDs/rGO heterostructure (Φ = 4.98 eV) compared to the isolated rGO (Φ = 5.21 eV) and CQDs (Φ = 5.29 eV) monolayers shown in Fig. 4(d–f). Compared to isolated materials, a reduction in the work function of naocomposite has been observed [49–51]. The reduced work function of CQDs/rGO heterostructure caused by synergistic electronic interactions between CQDs and rGO monolayers is expected to promote rapid generation of electrons-hole pairs compared to individual components toward achieving the enhanced photocatalytic activity.

3.3. Photocatalytic activity of CQDs/rGO catalyst

3.3.1. Photocatalytic degradation of MB dye

The photocatalytic degradation of MB dye (basic dye) via a CQDs/rGO catalyst (for 2 mg) using UV–Visible absorption spectra is shown in Fig. 5(a) and the plot of C/C_0 versus time is displayed in Fig. 5(b). The absorption spectrum of MB dye showed two peaks at 663 nm and 612 nm respectively corresponding to a n-π* and π-π* transition (vibronic transition) [52]. It was noticed that the absorbance of peak at 663 nm is decreased with increment in time for all the catalysts, and it completely vanished at 40 min for CQDs/rGO catalyst. The photocatalytic mechanism of CQDs/rGO catalysts for the degradation of MB dye can be explained as follows. The CQDs in CQDs/rGO catalyst produces electron in the LUMO state and holes in the HOMO state under visible light. Consequently, the electrons in the LUMO state of CQDs will easily transfered to the rGO by the good interface between CQDs and rGO. The restored sp^2 domains of rGO sheets will transfer these photogenerated electrons by convenient extra path thereby decreasing the radiative recombination rate as explained in the PL section. These photogenerated electrons will react with electron acceptors such as oxygen molecule and facilitates the formation of $O_2^{\bullet-}$ radicals. The produced $O_2^{\bullet-}$ radicals are powerful oxidizing agents and degrade the MB dye effectively under visible light. The additional reason for the improved photocatalytic activity of CQDs/rGO was attributed to its higher surface area as studied by BET method (The surface area of rGO, CQDs and CQDs/rGO was found to be 115 m^2/g 208 m^2/g and 296 m^2/g respectively). The increase in surface area of CQDs/rGO was due to anchoring of CQDs on rGO sheets which prevents its restacking. Further, the rGO sheets may avoid the agglomeration of CQDs which in turn increased the surface area provided by CQDs in CQDs/rGO nanocomposite, resulting in the increased adsorption of MB molecules on its catalyst, thus enhancing its photocatalytic activity. Furthermore, CQDs/rGO catalyst exhibited reduction in work function compared to CQDs and rGO as studied by DFT analysis in Section 3.2. The reduced work function of CQDs/rGO revealed the rapid generation of electrons-hole pairs compared to individual components results in enhanced visible light catalytic activity. The synergistic effects such as increase in surface area, and decrease in

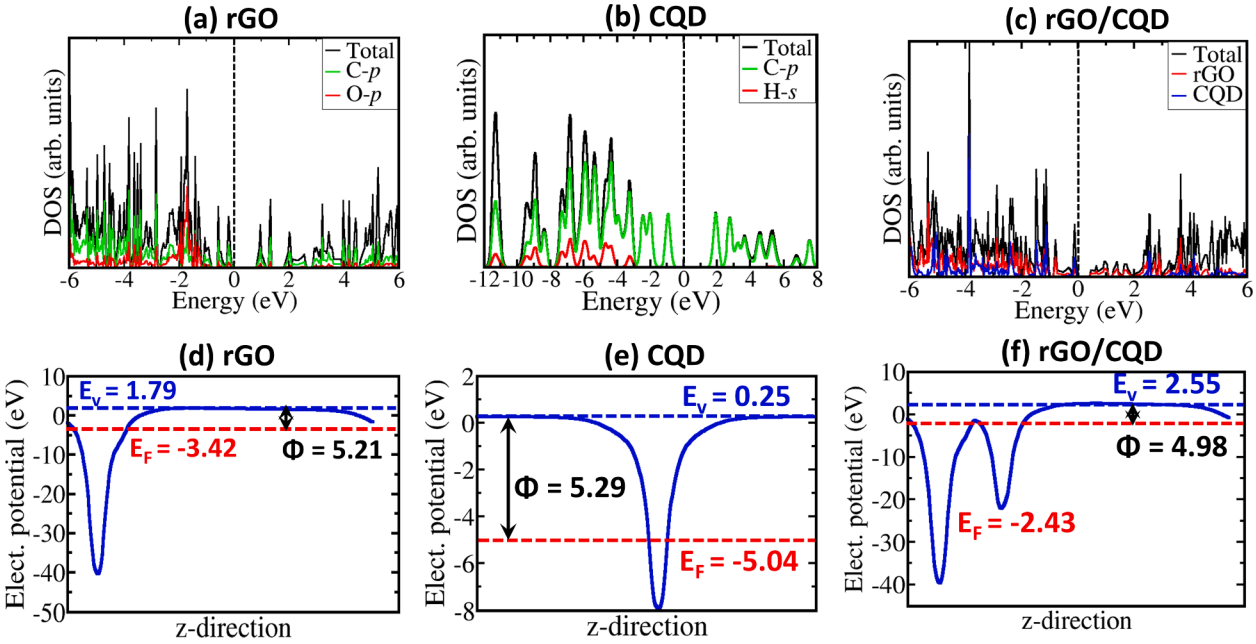

Fig. 4. The projected density pf states (a–c) and electrostatic potentials (e–f) of rGO, CQDs, and CQDs/rGO, respectively. E_v, E_F, and Φ in eV denotes the vacuum level, Fermi level, and work function.

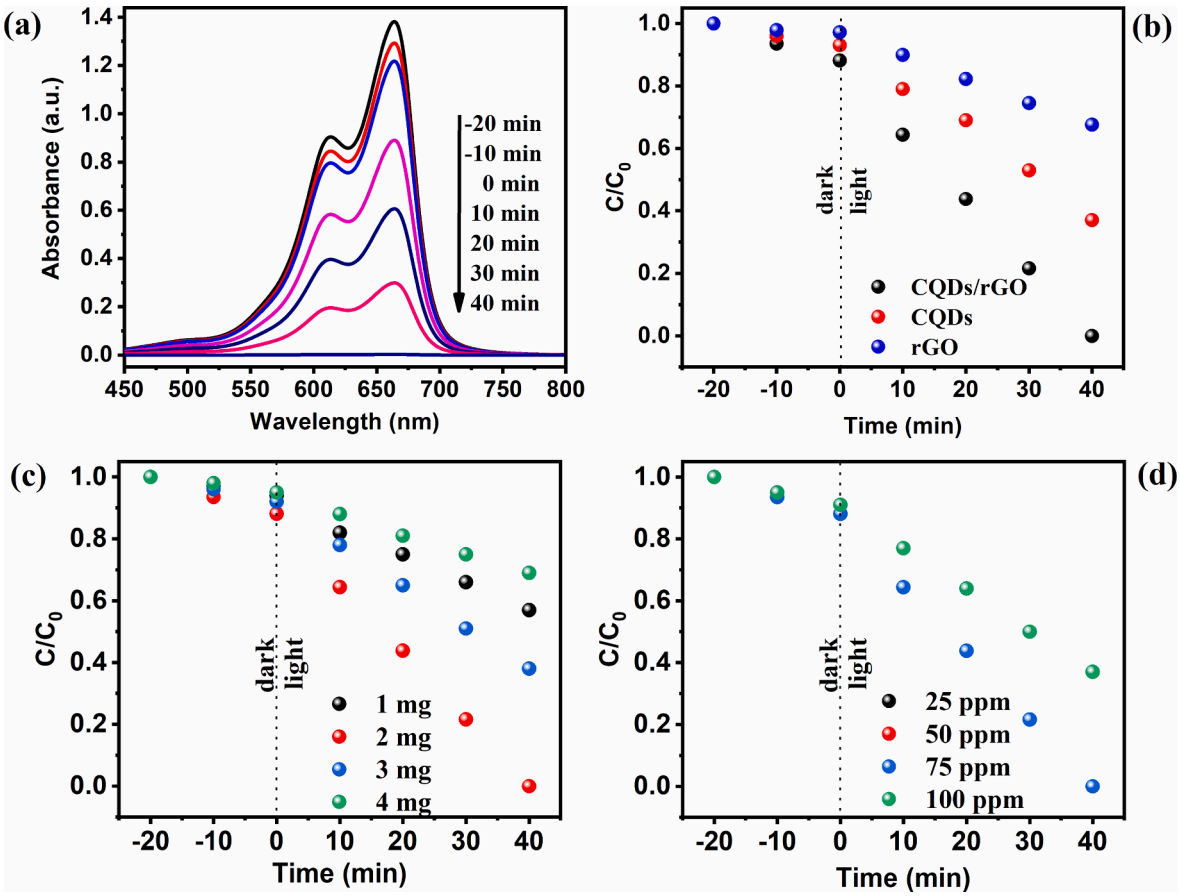

Fig. 5. (a) UV–Visible absorption degradation of MB dye (concentration of 75 ppm) by CQDs/rGO; (b) Plot of C/C_0 versus time of CQDs/rGO, CQDs and rGO; (c) Plot of C/C_0 versus time for different weights of CQDs/rGO catalyst; (d) Plot of C/C_0 versus time of CQDs/rGO catalysts at different concentration of MB dye. (C is concertation of (MB dye + catalyst) at time 't' min and C_0 is concentration of MB dye at time '0' min).

radiative recombination as well as work function leads to enhanced photocatalytic activity of CQDs/rGO. It is interesting to observe from Fig. 5(b) that the CQDs/rGO depicted enhanced photocatalytic performance compared to individual components such as CQDs and rGO due to synergistic effects as explained above.

In order to study the effect of catalyst loading on photocatalytic activity, different weights such as 1, 2, 3 and 4 mg of CQDs/rGO were added separately, and photocatalytic processes were carried out. The corresponding plots of C/C_0 versus time is shown in Fig. 5(c). It is noteworthy to observe that the percentage of MB dye degradation was 44%, 100%, 63% and 31% for 1, 2, 3 and 4 mg respectively at the end of 40 min. The photocatalytic activity was found to be less for 1 mg catalyst due to insufficient availability of active sites provided by the catalyst to the adsorption of MB dye molecules. Further, the percentage of MB dye degradation was found to be less for 3 mg and 4 mg of CQDs/rGO catalyst which is due to the blocking of active sites leading to obstruction of light, further restricting the effective photo generation of electrons and holes pair in the photocatalyst.

In order to study the effect of initial concentration on degradation of the MB dye, the photocatalytic experiments were carried out with concentrations of 25, 50, 75 and 100 ppm using 2 mg of CQDs/rGO catalyst. The corresponding plot of C/C_0 for different MB dye initial concentration versus time is depicted in Fig. 5(d). It is significant to witness that the percentage of degradation was found to be 100%, 100%, 100% and 63% for 25, 50, 75 and 100 ppm of MB respectively at the end of 40 min. This indicates that CQDs/rGO catalyst affords sufficient active sites for the adsorption of MB dye till 75 ppm and thereafter the decrease in percentage of degradation for 100 ppm of MB dye was due to the reduced adsorption active sites of catalyst.

The stability check of CQDs/rGO catalyst (2 mg) towards the photocatalytic degradation of MB dye (75 ppm) was studied. After the complete degradation of MB dye, the remaining solution was centrifuged and the obtained precipitate was dialyzed against Milli-Q water as explained in the experimental section. XRD was carried out for the obtained catalyst to confirm CQDs/rGO and is shown in Fig. S2(a). Then, under identical conditions, 2 mg of obtained catalyst was added to 100 ml of MB dye and photocatalytic activity was examined as explained in Section 2.5. The percentage of dye degradation versus cycle number is displayed in Fig. S2(b). For the initial cycle, CQDs/rGO catalyst exhibited the percentage of dye degradation as 99.92% and also it showed considerable percentage of dye degradation of 91.64% even after 7th cycle. XRD pattern of CQDs/rGO nanocomposite after 7th cycle is as shown in Fig. S2(a).

3.3.2. *Photocatalytic degradation of MO dye*

The photocatalytic degradation of MO dye (acidic dye) by CQDs/rGO catalyst (for 2 mg) is shown in UV–Visible absorption spectra of Fig. 6(a) and the plot of C/C_0 for different catalysts versus time is displayed in Fig. 6(b). The absorption spectrum of MO dye showed a strong peak around 450 nm due to the n-π* transition [53]. It is noticed that the absorbance of this peak decreased with increment in time for all the catalysts, and it completely vanished at 50 min for CQDs/rGO catalyst. The photocatalytic mechanism of CQDs/rGO catalysts for the degradation of MO dye was due to photogenerated electrons and holes, and subsequent generation $O_2^{\bullet-}$ radicals via rGO as explained in Section 3.3.1. These $O_2^{\bullet-}$ radicals degrade the MO dye under visible light as they are strong oxidizing agents. This enhancement in photocatalytic degradation of MO dye by CQDs/rGO was also supported by decrease in

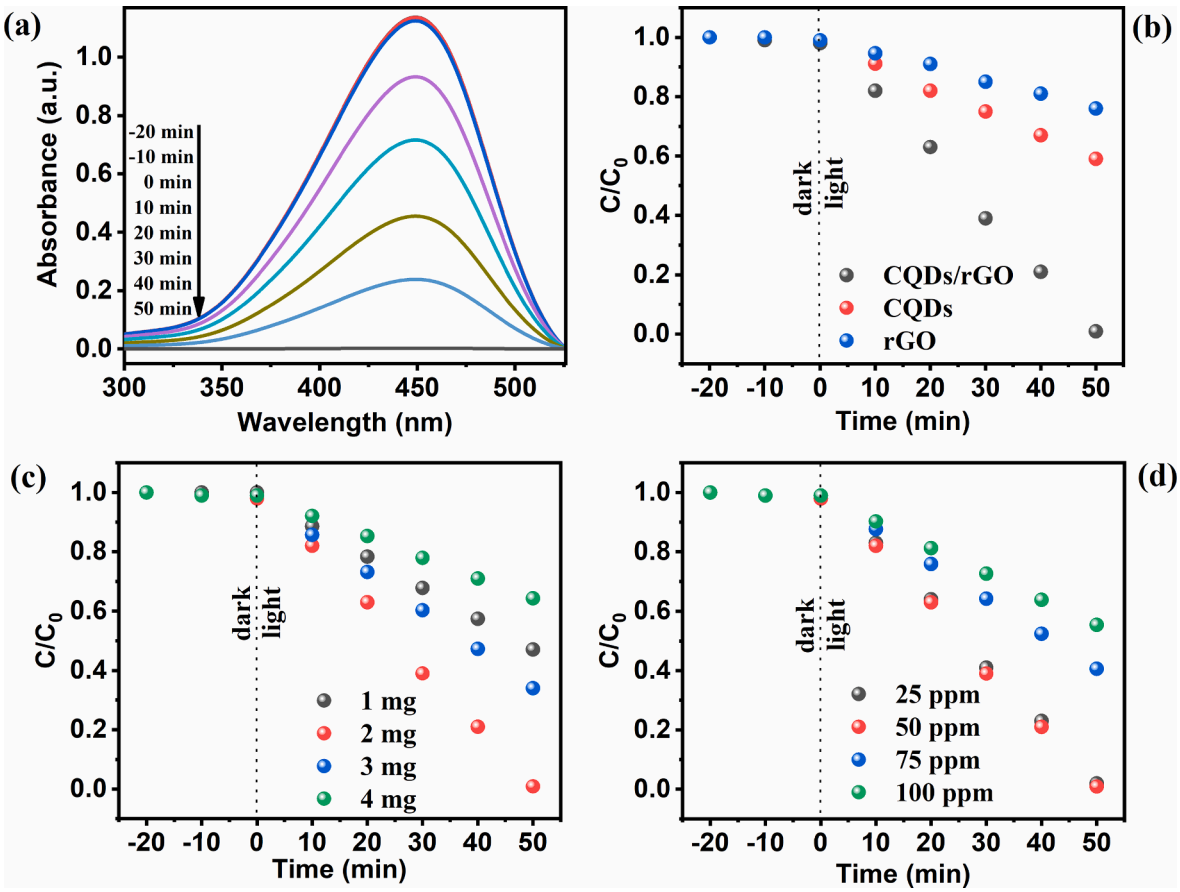

Fig. 6. (a) UV–Visible absorption degradation of MO dye (concentration of 50 ppm) by CQDs/rGO; (b) Plot of C/C_0 versus time of CQDs/rGO, CQDs and rGO; (c) Plot of C/C_0 versus time for different weights of CQDs/rGO catalyst; (d) Plot of C/C_0 versus time of CQDs/rGO catalysts at different concentration of MO dye. (C is concertation of (MO dye + catalyst) at time 't' and C_0 is concentration of MO dye at time '0').

radiative recombination and increase in surface area as explained in Section 3.3.1. Moreover, according to our study of CQDs/rGO by DFT analysis towards the decrement in work function, the rapid generation of electrons compared to their individual components results in enhanced visible light catalytic activity. The synergistic effects such as increase in surface area, and decrease in radiative recombination as well as work function leads to enhanced photocatalytic activity of CQDs/rGO. It is noteworthy to observe from Fig. 6(b) that the CQDs/rGO showed better photocatalytic performance towards MO dye degradation than that of individual components such as CQDs and rGO due to synergistic effects as explained above.

The effect of catalyst loading on photocatalytic activity was studied using different weights such as 1, 2, 3 and 4 mg of CQDs/rGO separately. The corresponding plots of C/C_0 versus time is depicted in Fig. 6(c), which showed the percentage of MO dye degradation as 92%, 100%, 91% and 85% for 1, 2, 3 and 4 mg respectively at the end of 50 min. The photocatalytic activity was found to be less for 1 mg catalyst due to insufficient availability of active sites provided by the catalyst to the adsorption of MO dye molecules. Further, the percentage of MO dye degradation was found to be less for 3 mg and 4 mg of CQDs/rGO catalyst which is due to the blocking of active sites leading to obstruction of light, further restricting the effective photo generation of electrons and holes pair in photocatalyst.

The effect of initial concentration of MO dye in photocatalytic activity of CQDs/rGO was studied by varying the concentrations such as 25, 50, 75 and 100 ppm using 2 mg of CQDs/rGO catalyst. The corresponding plot of C/C_0 for different initial concentration of MB dye is depicted in Fig. 6(d) and its showed the percentage of degradation of MO dye as 100%, 100%, 100% and 93% for 25, 50, 75 and 100 ppm respectively at the end of 50 min. This reveals that CQDs/rGO catalyst affords sufficient active sites for the adsorption of MB dye till 75 ppm and thereafter the decrease in percentage of degradation for 100 ppm of MB dye was due to the reduced adsorption active sites of catalyst.

The stability check of CQDs/rGO catalyst (2 mg) for the photocatalytic degradation of MO dye (50 ppm) was studied. The catalyst was recovered as explained in Section 3.3.1 and confirmed by XRD, as shown in Fig. S3(a). Then, 2 mg of obtained catalyst was added to 100 ml of MO dye and photocatalytic activity was repeated under identical condition. The percentage of dye degradation for different cycle number is displayed in Fig. S3(b). For the initial first cycle, CQDs/rGO catalyst exhibited the percentage of dye degradation as 99.94% and it showed substantial percentage of dye degradation of 90.15% even after 7th cycle. XRD pattern of CQDs/rGO after 7th cycle of degradation is shown in Fig. S3(a).

3.3.3. *Reaction kinetics of photocatalytic activity of CQDs/rGO*

The reaction kinetics was studied using pseudo first order kinetics equation which is given by [31], $Ln\left(\frac{C}{C_0}\right) = -kt$, where C_0 and C are initial and final concentration at a time "t" respectively and k being a reaction rate constant in the equation. The plot of $Ln\left(\frac{C}{C_0}\right)$ versus time "t" for catalysts (2 mg) such as CQDs/rGO, rGO and CQDs for the MB (75 ppm) and MO (50 ppm) photocatalytic degradation is displayed in Fig. 7 (a) & (b). The obtained reaction rate constants of CQDs/rGO, CQDs and rGO catalysts were found to be (i) 0.352 min^{-1}, 0.176 min^{-1} and 0.081 min^{-1} respectively for MB degradation and (ii) 0.118 min^{-1}, 0.079 min^{-1} and 0.053 min^{-1} respectively for MO degradation. It is worth to

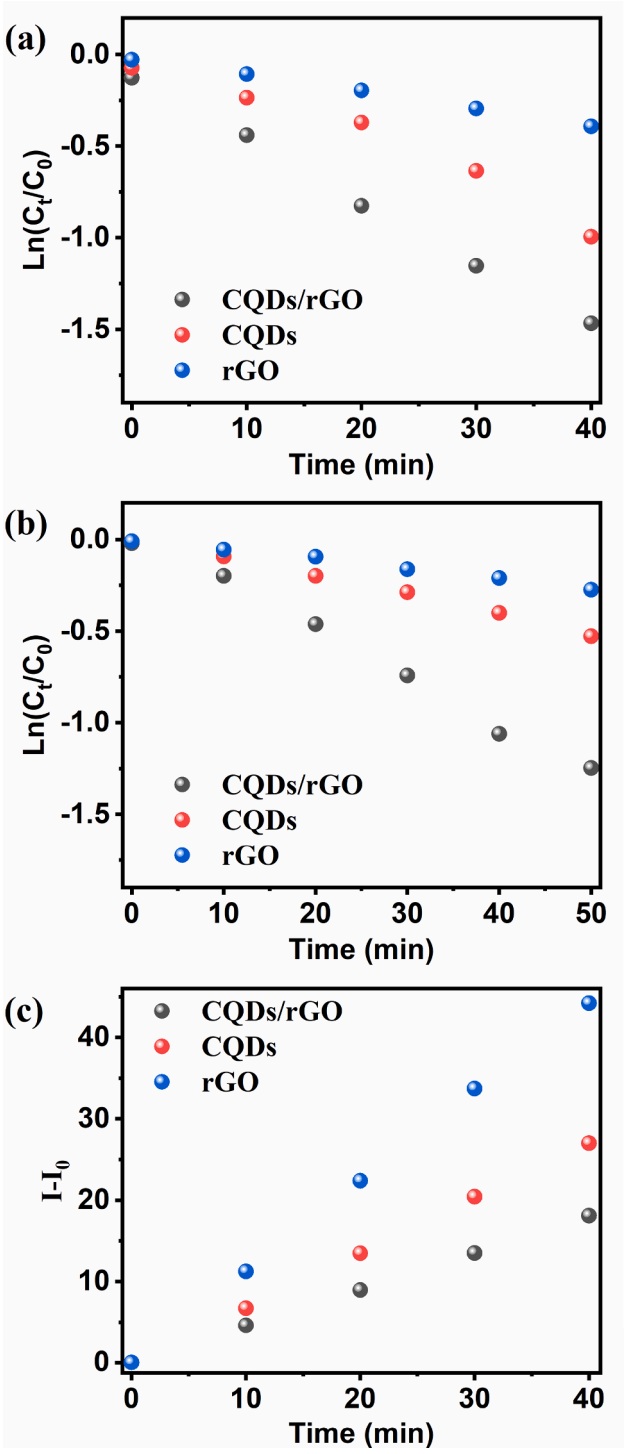

Fig. 7. Plot of $Ln(C_t/C_0)$ versus time (min) of catalysts for (a) MB dye, (b) MO dye; (c) Fluorescence intensity versus visible light irradiation time for different catalysts.

mention that CQDs/rGO catalyst showed large reaction constant both in cases of MB and MO degradation revealing the enhanced efficiency of photocatalytic activity due to synergetic effects of individual components, which results in increase in surface area and decrease in radiative recombination as well as the reduced work function. It is also clearly observed that the CQDs/rGO catalyst showed a higher reaction rate constant for MB degradation than that of MO degradation, due to the high quantum yield and enhanced surface states of CQDs in basic environment [54]. Arguably, the obtained results reveal that the CQDs/rGO catalyst developed by sonochemical assisted method can be applied for the photo degradation of both basic dye (MB) and acidic dye (MO) under visible light.

Also, during photocatalytic degradation process, CQDs in CQDs/rGO catalyst generated electrons and holes under visible light. The so generated holes may produce •OH radicals, which can also degrade MB and MO dye [54]. To confirm the formation of •OH radicals, terephthalic acid probe experiment, in which terephthalic acid reacts with •OH radical forming 2-hydroxyterephthalic acid was carried out. 2-hydroxyterephthalic acid exhibits unique fluorescence centered at 426 nm when excited at 312 nm [54]. Fig. 7(c) shows the plot of fluorescence signals versus visible light irradiation time for CQDs/rGO, CQDs and rGO catalysts. It can be observed that CQDs/rGO catalyst have better efficiency of formation of •OH radicals than that of CQDs and rGO suggesting its enhanced photocatalytic activity.

4. Conclusions

The CQDs of size (2–5) nm were anchored on rGO sheets by sonochemical assisted method. CQDs/rGO catalyst showed enhancement in photocatalytic activity towards the degradation of MB as well as MO dyes due to synergistic effect of individual components, which results in disruptive radiative recombination and upsurge in surface area as studied by PL and BET method respectively. The improved photocatalytic activity of CQDs/rGO catalyst was also corroborated by increase in density of states thereby decrease in work function as studied by first principles density functional theory calculations.

CRediT authorship contribution statement

M.G. Ashritha: Methodology, Investigation, Writing - original draft. **Sachin R. Rondiya:** Software, Formal analysis. **Russell W. Cross:** Software, Formal analysis. **Nelson Y. Dzade:** Software, Formal analysis. **S.D. Dhole:** Resources. **K. Hareesh:** Conceptualization, Methodology, Validation, Writing - review & editing, Supervision, Funding acquisition. **D.V. Sunitha:** Methodology.

Declaration of Competing Interest

The authors declare that they have no known competing financial interests or personal relationships that could have appeared to influence the work reported in this paper.

Acknowledgements

Authors acknowledges Prof. S.M. Shivaprasad from JNCASR, Bengaluru for providing TEM and XPS facilities. One of the authors, KH acknowledges SERB-ECR, Govt. of India (File No. ECR/2017/002788) for supporting the work. S.R.R, R.W.C, and N.Y.D acknowledge the UK Engineering and Physical Sciences Research Council (EPSRC) for funding (Grant No. EP/S001395/1). This work has also used the computational facilities of the Advanced Research Computing at Cardiff (ARCCA) Division, Cardiff University, and HPC Wales. This work also made use of the facilities of ARCHER (http://www.archer.ac.uk), the UK's national supercomputing service via the membership of the UK's HEC Materials Chemistry Consortium, which is funded by EPSRC (EP/L000202). Information on the data that underpins the results presented here, including how to access them, can be found in the Cardiff University data catalogue at http://doi.org/10.17035/d.2021.0126100872.

Appendix A. Supplementary material

Supplementary data to this article can be found online at https://doi.org/10.1016/j.apsusc.2021.148962.

References

[1] Y. Wang, A. Hu, Carbon quantum dots: synthesis, properties and applications, J. Mater. Chem. C 2 (2014) 6921–6939.
[2] M.L. Liu, B.B. Chen, C.M. Li, C.Z. Huang, Carbon dots: synthesis, formation mechanism, fluorescence origin and sensing applications, Green Chem. 21 (2019) 449–471.
[3] P. Wu, C. Zhou, Y. Li, M. Zhang, P. Tao, Q. Liu, W. Cui, Flower-like FeOOH hybridized with carbon quantum dots for efficient photo-Fenton degradation of organic pollutants, Appl. Surf. Sci. 540 (2021), 148362.
[4] H.J. Yashwanth, S.R. Rondiya, N.Y. Dzade, S.D. Dhole, D.M. Phase, K. Hareesh, Enhanced photocatalytic activity of N, P, co-doped carbon quantum dots: an insight from experimental and computational approach, Vacuum 180 (2020), 109589.
[5] S. Yang, J. Sun, X. Li, W. Zhou, Z. Wang, P. He, G. Ding, X. Xie, Z. Kang, M. Jiang, Large-scale fabrication of heavy doped carbon quantum dots with tunable-photoluminescence and sensitive fluorescence detection, J. Mater. Chem. A 2 (2014) 8660–8667.
[6] P. Mirtchev, E.J. Henderson, N. Soheilnia, C.M. Yip, G.A. Ozin, Solution phase synthesis of carbon quantum dots as sensitizers for nanocrystalline TiO_2 solar cells, J. Mater. Chem. 22 (2012) 1265–1269.
[7] J. Zhao, F. Li, S. Zhang, Y. An, S. Sun, Preparation of N-doped yellow carbon dots and N, P co-doped red carbon dots for bioimaging and photodynamic therapy of tumors, New J. Chem. 43 (2019) 6332–6342.
[8] M.J. Molaei, Carbon quantum dots and their biomedical and therapeutic applications: a review, RSC Adv. 9 (2019) 6460–6481.
[9] P. Wu, W. Li, Q. Wu, Y. Liu, S. Liu, Hydrothermal synthesis of nitrogen-doped carbon quantum dots from microcrystalline cellulose for the detection of Fe^{3+} ions in an acidic environment, RSC Adv. 7 (2017) 44144–44153.
[10] S. Mitra, S. Chandra, S.H. Pathan, N. Sikdar, P. Pramanik, A. Goswami, Room temperature and solvothermal green synthesis of self-passivated carbon quantum dots, RSC Adv. 3 (2013) 3189–3193.
[11] Y. Dong, N. Zhou, X. Lin, J. Lin, Y. Chi, G. Chen, Extraction of electro chemiluminescent oxidized carbon quantum dots from activated carbon, Chem. Mater. 22 (2010) 5895–5899.
[12] Y.P. Sun, B. Zhou, Y. Lin, W. Wang, K.S. Fernando, P. Pathak, M.J. Meziani, B. A. Harruff, X. Wang, H. Wang, Quantum-sized carbon dots for bright and colorful photoluminescence, J. Am. Chem. Soc. 128 (2006) 7756–7757.
[13] Y. Choi, S. Jo, A. Chae, Y.K. Kim, J.U. Park, D. Lim, S.Y. Park, I. In, Simple microwave-assisted synthesis of amphiphilic carbon quantum dots from A_3/B_2 polyamidation monomer set, ACS Appl. Mater. Interfaces 9 (2017) 27883–27893.
[14] H. Dang, L.K. Huang, Y. Zhang, C.F. Wang, S. Chen, Large-scale ultrasonic fabrication of white fluorescent carbon dots, Ind. Eng. Chem. Res. 55 (2016) 5335–5341.
[15] H. Xu, B.W. Zeiger, K.S. Suslick, Sonochemical synthesis of nanomaterials, Chem. Soc. Rev. 42 (2013) 2555–2567.
[16] R. Liu, D. Wu, S. Liu, K. Koynov, W. Knoll, Q. Li, An aqueous route to multicolor photoluminescent carbon dots using silica spheres as carriers, Angew. Chem. Int. Ed. 48 (2009) 4598–4601.
[17] H. Li, X. He, Y. Liu, H. Huang, S. Lian, S.T. Lee, Z. Kang, One-step ultrasonic synthesis of water-soluble carbon nanoparticles with excellent photoluminescent properties, Carbon 49 (2011) 605–609.
[18] V.B. Kumar, Z. Porat, A. Gedanken, Facile one-step sonochemical synthesis of ultrafine and stable fluorescent C-dots, Ultrason. Sonochem. 28 (2016) 367–375.
[19] M. Maruthapandi, A. Gedanken, A short report on the polymerization of pyrrole and its copolymers by sonochemical synthesis of fluorescent carbon dots, Polymers (Basel) 11 (2019) 23–29.
[20] V.B. Kumar, J. Tang, K.J. Lee, V.G. Pol, A. Gedanken, In situ sonochemical synthesis of luminescent Sn@C-dots and a hybrid Sn@C-dots@Sn anode for lithium-ion batteries, RSC Adv. 6 (2016) 66256–66265.
[21] V.B. Kumar, R. Kumar, A. Gedanken, O. Shefi, Fluorescent metal-doped carbon dots for neuronal manipulations, Ultrason. Sonochem. 52 (2019) 205–213.
[22] K. Wei, J. Li, Z. Ge, Y. You, H. Xu, Sonochemical synthesis of highly photoluminescent carbon nanodots, RSC Adv. 4 (2014) 52230–52234.
[23] S.J. Phang, L.L. Tan, Recent advances in carbon quantum dot (CQD)-based two dimensional materials for photocatalytic applications, Catal. Sci. Technol. 9 (2019) 5882–5905.
[24] Y. Zhu, S. Murali, W. Cai, X. Li, J.W. Suk, J.R. Potts, R.S. Ruoff, Graphene and graphene oxide: synthesis, properties, and applications, Adv. Mater. 22 (2010) 3906–3924.
[25] R. Tarcan, O.T. Boer, I. Petrovai, C. Leordean, S. Astilean, I. Botiz, Reduced graphene oxide today, J. Mater. Chem. C 8 (2020) 1198–1224.
[26] S.J. Rowley-Neale, E.P. Randviir, A.S.A. Dena, C.E. Banks, An overview of recent applications of reduced graphene oxide as a basis of electroanalytical sensing platforms, Appl. Mater. Today 10 (2018) 218–226.
[27] T. Soltani, B.K. Lee, A benign ultrasonic route to reduced graphene oxide from pristine graphite, J. Colloid Interface Sci. 486 (2017) 337–343.
[28] S.K. Arumugasamy, P. Kanagavalli, M. Veerapandian, M. Jayaraman, K. Yun, Electrochemical properties of Rubpy-reduced graphene oxide synergized by ultrasonication for label-free quercetin sensing, Appl. Surf. Sci. 537 (2021), 147777.
[29] D.H. Shin, C.W. Jang, J.S. Ko, S.H. Choi, Enhancement of efficiency and stability in organic solar cells by employing MoS_2 transport layer, graphene electrode, and graphene quantum dots-added active layer, Appl. Surf. Sci. 538 (2021), 148155.
[30] N. Sharma, S.P. Selvam, K. Yun, Electrochemical detection of amikacin sulphate using reduced graphene oxide and silver nanoparticles nanocomposite, Appl. Surf. Sci. 512 (2020), 145742.
[31] J. Li, C. Bing, W. Jun, L. Xiaoying, H. Ailin, J. Qi, High pressure homogenization treatment on graphene oxide and its electrochemical energy storage performance, Appl. Surf. Sci. 493 (2019) 441–447.
[32] A. Raja, P. Rajasekaran, K. Selvakumar, M. Arivanandhan, S.A. Bahadur, M. Swaminathan, Rational fabrication of needle with spherical shape ternary reduced Graphene Oxide-$HoVO_4$-TiO_2 photocatalyst for degradation of ibuprofen under visible light, Appl. Surf. Sci. 513 (2020), 145803.
[33] J. Li, X. Yun, Z. Hu, L. Xi, N. Li, H. Tang, P. Lu, Y. Zhu, Three-dimensional nitrogen and phosphorus co-doped carbon quantum dots/reduced graphene oxide composite aerogels with hierarchical porous structure as superior electrode materials for supercapacitors, J. Mater. Chem. A 7 (2019) 26311–26325.
[34] C. Zheng, L. Huang, Q. Guo, W. Chen, W. Li, H. Wang, Facile one-step fabrication of upconversion fluorescence carbon quantum dots anchored on graphene with enhanced nonlinear optical responses, RSC Adv. 8 (2018) 10267–10276.
[35] M. Zhao, J. Zhang, H. Xiao, T. Hu, J. Jia, H. Wu, Facile in situ synthesis of a carbon quantum dot/graphene heterostructure as an efficient metalfree electrocatalyst for overall water splitting, Chem. Commun. 55 (2019) 1635–1638.
[36] K. Hareesh, B. Shateesh, R.P. Joshi, S.S. Dahiwale, V.N. Bhoraskar, S.K. Haram, S. D. Dhole, PEDOT:PSS wrapped $NiFe_2O_4$/rGO tertiary nanocomposite for the super-capacitor applications, Electro. Acta 201 (2016) 106–116.
[37] G. Kresse, J. Hafner, Ab initio molecular dynamics for liquid metals, Phys. Rev. B 47 (1993) 558.
[38] G. Kresse, D. Joubert, From ultrasoft pseudopotentials to the projector augmented-wave metho, Phys. Rev. B 59 (1999) 1758.
[39] G. Kresse, J. Furthmüller, Efficient iterative schemes for ab initio total-energy calculations using a plane-wave basis set, Phys. Rev. B 54 (16) (1996) 11169.
[40] P. E. Blöchl, Projector augmented-wave method, Phys. Rev. B 50.24 (1994) 17953. J. Chem. Phys. 125 (2006) 224106.
[41] V. Krukau, O.A. Vydrov, A.F. Izmaylov, G.E. Scuseria, Influence of the exchange screening parameter on the performance of screened hybrid functionals, J. Chem. Phys. 125 (2006), 224106.
[42] J.P. Perdew, K. Burke, M. Ernzerh, Generalized gradient approximation made simple, Phys. Rev. Lett. 78 (1997) 1396.
[43] P.E. Blöchl, O. Jepsen, O.K. Andersen, Improved tetrahedron method for Brillouin-zone integrations, Phys. Rev. B 49 (1994) 16223.
[44] N. Karikalan, R. Karthik, S.M. Chen, C. Karuppiah, A. Elangovan, Sonochemical synthesis of sulfur doped reduced graphene oxide supported CuS nanoparticles for the non-enzymatic glucose sensor applications, Sci. Rep. 7 (2017) 2494.
[45] K. Hareesh, R.P. Joshi, B. Shateesh, K. Asokan, D. Kanjilal, D.J. Late, S.S. Dahiwale, V.N. Bhoraskar, S.K. Haram, S.D. Dhole, Reduction of graphene oxide by 100 MeV Au ion irradiation and its application as H_2O_2 sensor, J. Phys. D: Appl. Phys. 48 (2015), 365105.
[46] Z.C. Yang, M. Wang, A.M. Yong, S.Y. Wong, X.H. Zhang, H. Tan, A.Y. Chang, X. Li, J. Wang, Intrinsically fluorescent carbon dots with tunable emission derived from hydrothermal treatment of glucose in the presence of monopotassium phosphate, Chem. Commun. 47 (2011) 11615–11617.
[47] K. Hareesh, R.P. Joshi, D.V. Sunitha, V.N. Bhoraskar, S.D. Dhole, Anchoring of Ag-Au alloy nanoparticles on reduced graphene oxide sheets for the reduction of 4-nitrophenol, Appl. Surf. Sci. 389 (2016) 1050–1055.
[48] F. Zheng, W.L. Xu, H.D. Jin, X.T. Hao, K.P. Ghiggino, Charge transfer from poly (3-hexylthiophene) to graphene oxide and reduced graphene oxide, RSC Adv. 5 (2015) 89515–89520.
[49] Sachin R. Rondiya, Indrapal Karbhal, Chandradip D. Jadhav, Mamta P. Nasane, Thomas Davies, Manjusha V. Shelke, Sandesh R. Jadkar, Padmakar G. Chavan, Nelson Y. Dzade, Uncovering the origin of enhanced field emission properties of rGO-MnO_2 heterostructure, RSC Adv. 10 (2020) 25988–25998.
[50] P.K. Baviskar, S.R. Rondiya, G.P. Patil, B.R. Sankapal, H.M. Pathan, P.G. Chavan, N.Y. Dzade, ZnO/CuSCN nano-heterostructure as a highly efficient field emitter: a combined experimental and theoretical investigation, ACS Omega 5 (2020) 6715–6724.
[51] S.R. Rondiya, C.D. Jadhav, P.G. Chavan, N.Y. Dzade, Enhanced field emission properties of Au/SnSe nano-heterostructure: a combined experimental and theoretical investigation, Sci. Rep. 10 (2020) 1–10.
[52] K. Hareesh, R.P. Joshi, S.S. Dahiwale, V.N. Bhoraskar, S.D. Dhole, Synthesis of Ag-reduced graphene oxide nanocomposite by gamma radiation assisted method and its photocatalytic activity, Vacuum 124 (2016) 40–45.
[53] M.U.D. Sheikh, G.A. Naikoo, M. Thomas, M. Bano, F. Khan, Solar-assisted photocatalytic reduction of methyl orange azo dye over porous TiO_2 nanostructures, New J. Chem. 40 (2016) 5483–5494.
[54] S. Hu, Z. Wei, Q. Chang, A. Trinchi, J. Yang, A facile and green method towards coal-based fluorescent carbon dots with photocatalytic activity, Appl. Surf. Sci. 378 (2016) 402–407.